


Article

Microstructural Evolution of Reaction Layer of 1.5 GPa Boron Steel Hot-Dipped in Al-7wt%Ni-6wt%Si Alloy

Jeong-Yong Lee, Hoejun Heo, Namhyun Kang *  and Chung-Yun Kang *

Department of Materials Science and Engineering, Pusan National University (PNU), Pusan 46241, Korea; jy689654@gmail.com (J.-Y.L.); hjheo@pusan.ac.kr (H.H.)

* Correspondence: nhkang@pusan.ac.kr (N.K.); kangcy@pusan.ac.kr (C.-Y.K.);
Tel.: +82-51-510-3274 (N.K.); +82-10-8329-8429 (C.-Y.K.)

Received: 13 November 2018; Accepted: 13 December 2018; Published: 15 December 2018



Abstract: The constituents, distribution, and characteristics of the phases formed on the coating layer of boron steel hot-dipped in Al-7wt%Ni-6wt%Si were evaluated in detail. In particular, the microstructure and phase constitution of the reaction layer were characterized. Moreover, the microstructural evolution mechanism of the phase was presented with reference to the (Al-7wt%Ni-6wt%Si)-xFe from the pseudo-binary phase diagram. The solidification layer consisted mainly of Al, Al₃Ni, and Si phases. Reaction layers were formed in the order of Al₉FeNi(T), Fe₄Al₁₃(θ), and Fe₂Al₅(η) from the solidification layer side. In addition, the κ (Fe₃AlC) layer was formed at the Fe₂Al₅(η)/steel interface. From pseudo-binary phase diagram analysis, it was found that Fe₄Al₁₃(θ) can form when the Fe concentration is over 2.63 wt% in the 690 °C Al-7wt%Ni-6wt%Si molten metal. When the concentration of Fe increased to 10.0–29.0 wt%, isothermal solidification occurred in the Fe₄Al₁₃(θ) and Al₉FeNi(T) phases simultaneously. Moreover, given that the T phase does not dissolve Si, it was discharged, and the Si phase was formed around the Al₉FeNi(T) phase. The Fe₂Al₅(η) phase was formed by a diffusion reaction between Fe₄Al₁₃(θ) and steel, not a dissolution reaction. Moreover, Al₂Fe₃Si₃(τ₁) was formed at the Fe₄Al₁₃(θ)-Fe₂Al₅(η) interface by discharging Si from Fe₄Al₁₃(θ) without Si solubility. Furthermore, the Fe₃AlC(κ) layer was formed by carbon accumulation that discharged in the Fe₂Al₅(η) region transformed from steel to Fe₂Al₅(η). The twin regions in the Fe₄Al₁₃(θ) and Fe₂Al₅(η) grain were due to the strains caused by the lattice transformation in the constrained state, wherein the phases are present between the Al₉FeNi(T) layer and steel.

Keywords: hot-dipping; intermetallics formation; diffusion; phase transformation

1. Introduction

In recent years, the automobile industry has been using boron steel, in which boron is added to a low alloy steel, for environmental friendliness, low fuel consumption, and low weight. When boron is added to steel, the boron is segregated in the previous austenite grain boundaries, even if only approximately 20 ppm is added, and the hardenability can be significantly improved by delaying the ferrite nucleation on cooling. Moreover, boron steel is boron-added low alloy steel, and it is a type of advanced high-strength steel (AHSS) with a tensile strength of 1.5 GPa [1]. Due to the high strength of boron steel, cold forming is difficult, and the spring-back phenomenon occurs after forming. Therefore, hot stamping is performed to maintain the ductility by heating to a temperature of A3 or higher, press forming, and rapid cooling to maintain a high strength. Hot stamping involves heating at a temperature of A3 or higher, to ensure ductility, and then quenching to maintain a high strength [2–5]. In hot stamping, surface oxidation and surface decarburization occur on heating at a high temperature;

therefore, it is mainly performed with Al-10%Si coating, which has an excellent oxidation resistance at high temperatures [6–8]. When the Al-Si hot-dipped boron steel was laser-welded, Al and Si segregation portions were formed in the fusion zone. The portion formed a ferrite with low hardness during hot stamping, and it was reported that the tensile properties of the fusion zone decreased [9–12]. In addition, Yoon et al. reported that a hook-shaped $\text{Fe}_3(\text{Al}, \text{Si})$ intermetallic compound was formed on the interface between the fusion zone and base metal during laser welding. Moreover, it was transformed to polygonal ferrite during the hot stamping processes, and the tensile properties were degraded [13].

There are several studies on the development of coating compositions for the inhibition of ferrite formation in Al-Si hot-dipped boron steel welding. Coating compositions were designed by adding Mn or Ni, which are austenite-forming elements, to Al. In general, research on the microstructures of Al-7wt%Mn [14] and the Al-7wt%Ni [15] coating layer was conducted. In the abovementioned studies, the desired Ni phase (Al_9FeNi) and Mn phase (Al_6Mn , $\text{Al}_{11}\text{Mn}_4$) were formed; however, the $\text{Fe}_2\text{Al}_5(\eta)$ phase layer, which is the cause of ferrite formation, was formed with a thickness of approximately 100 μm .

On the other hand, when Si is added to a molten bath when hot-dipping the carbon steel and low alloy steel, the thickness of the produced intermetallic compound $\text{Fe}_2\text{Al}_5(\eta)$ phase during plating can be reduced. In addition, the melting point and viscosity of the molten bath can be reduced to increase the coating ability [16–18]. Several mechanisms were proposed to explain the decrease in the thickness of the $\text{Fe}_2\text{Al}_5(\eta)$ phase due to the addition of Si, such as an Al diffusion delay due to the Si solubility in the $\text{Fe}_2\text{Al}_5(\eta)$ phase vacancy [16,19], Al diffusion delay due to the Si segregated in the $\text{Fe}_2\text{Al}_5(\eta)$ phase grain boundary [20], and a reduction in the Al activation coefficient due to the addition of Si [21,22]. In most studies, it was reported that Si inhibits the growth of the $\text{Fe}_2\text{Al}_5(\eta)$ phase by reducing the diffusion and activation coefficients of Al. On the other hand, Lemmens B. et al. reported that the amount and thickness of the Al-Fe-Si ternary phase (τ_1 , τ_5) generated in the $\text{Fe}_2\text{Al}_5(\eta)$ phase increased and the thickness of the $\text{Fe}_2\text{Al}_5(\eta)$ phase decreased when the amount of Si added to the coating bath was increased [23].

Yun et al. reported that the thickness of the $\text{Fe}_2\text{Al}_5(\eta)$ phase decreased and the amount of the $\text{Al}_9\text{FeNi}(\text{T})$ phase (which they think that inhibiting ferrite formation phase when welding) increased as the amount of Si increased through hot-dip coating with (1–6) wt%Si added to Al-7wt%Ni [24]. In particular, it was reported that due to the addition of Si, 1–5 at% of Si was dissolved in the η phase to interfere with the growth of Al. Moreover, the $\text{Al}_2\text{Fe}_3\text{Si}_3(\tau_1)$ phase was generated, and it preferentially consumed Al. However, there was no mention of the formation of a reaction layer during the coating, the characteristics, and formation mechanism of the reaction phases.

Given that the $\text{Fe}_2\text{Al}_5(\eta)$ phase of the reaction layer that contains a minimum of 5 wt% of Si during the hot-dip coating of the Al alloy is 2 μm or lower in thickness, and the grain diameter of the Al-Fe-Si ternary phase (τ_1 , τ_5) is 1 μm or lower, studies that employ transmission electron microscopy (TEM) are required. However, in most studies, only X-ray diffraction (XRD), energy-dispersive X-ray spectroscopy (EDS), and electron backscatter diffraction (EBSD) analyses were conducted; thus, the accuracy of the analyses was limited. In addition, there are no reports on the formation of carbon-related phases during the coating of steels that contain a certain amount of carbon, such as boron steel (0.22 wt% of carbon).

Hence, in this study, the reaction layer formed on the boron steel coated at 690 °C for 2 min in an Al-7wt%Ni-6wt%Si molten bath was deflected by a focused ion beam (FIB), and phase identification was conducted using TEM and TEM-EDS. Moreover, Electron Backscatter Diffraction (EBSD) was used for the microstructure analysis of the macroscopic reaction layer and solidification layer. The mechanism of formation of intermetallic compounds was further investigated using a pseudo-binary phase diagram.

2. Materials and Methods

The base metal used in this study was boron steel (22MnB5) with a thickness of 1.4 mm, for which the chemical composition is presented in Table 1. The Al-7wt%Ni-6wt%Si alloy was prepared by appropriately mixing high-purity (99.99%) Al ingot, high-purity (99.99%) Al-15wt%Si ingot, and high-purity (99.99%) Ni ingot. The specimens to be coated were cut to a size of 40 mm × 120 mm, pickled in a solution that consisted of 40 mL of H₂SO₄ and 200 mL of CH₃OH for 5 min, and then rinsed using C₂H₅OH.

Table 1. Chemical composition (wt%) of Boron steel.

| C | Si | Mn | Cr | Nb | Ti | B | P | S | Fe |
|--------|--------|--------|--------|--------|--------|--------|--------|--------|------|
| 0.2285 | 0.2383 | 1.1890 | 0.1833 | 0.0036 | 0.0363 | 0.0023 | 0.0015 | 0.0015 | Bal. |

The prepared hot-dip coated alloy was heated in a crucible set in a high-frequency furnace, and then maintained at a coating temperature of 690 °C for melting. The pre-treated specimens were pre-heated at 150 °C for 20 s to remove moisture from the surface, and then placed in a molten bath of Al-7wt%Ni-6wt%Si, which was maintained at 690 °C for 2 min for coating. After coating, the specimens were cooled in air.

The coated specimens were polished in the normal direction using #180–2500 SiC sandpaper, a 1 µm diamond suspension, and a 0.04 µm colloidal silica suspension. The coating layer was then etched using 49 mL of distilled water and 1 mL of HF according to ASTM B487-85. The etched coating layer was observed using an optical microscope (Olympus BX51M; Tokyo, Japan) and field-emission scanning electron microscopy (FE-SEM) system (Carl Zeiss SUPRA 45; Oberkochen, Germany). Moreover, EDS (EDAX; Mahwah, NJ, USA) and field-emission electron probe micro-analysis (FE-EPMA) (JEOL JXA-8530F; Tokyo, Japan) were performed to analyze the composition of the coating layer. For FE-EPMA, area analysis was conducted with a voltage of 10 kV, a current of 100 nA, and step sizes of 0.1–0.5 mm in the non-etched state.

For the phase analysis of the reaction layer, the TEM specimens were deflected using FIB (FEI, Scios; Hillsboro, OR, USA). The diffraction pattern and chemical composition were analyzed using FE-TEM (FEI, TALOS F200X; Hillsboro, OR, USA). In addition, EBSD (EDAX, Hikari; Mahwah, NJ, USA) was used for the phase distribution and crystal orientation analyses. In particular, phase distributions were confirmed by Chi-Scanning that using EDS and EBSD. The thickness and length of the reaction layer were measured using the Image-Plus Pro image analysis program. The equilibrium composition of each phase formed during the coating and the (Al-7wt%Ni-6wt%Si)-xFe pseudo-binary phase diagram were obtained using Thermo-CalcTM software Ver. 6.0 (Solna, Sweden), for the evaluation of the formation mechanism of each phase.

3. Results and Discussion

3.1. Microstructure of Solidification Layer

3.1.1. Identification of Solidification Layer Phases

Figure 1 presents the structure of the specimen coated at 690 °C for 2 min in an Al-7wt%Ni-6wt%Si molten bath, as observed using the optical microscope. The coating layer was classified into a solidification layer (SL) and reaction layer (RL). Reaction layer (RL) is boron-steel/coating layer interface that composed of gray layers that observed some black particles inside and ivory phases that attached to gray layer and grown to solidification layer.

The second phases in the solidification layer were mainly formed on the grain (or dendrite) boundary.

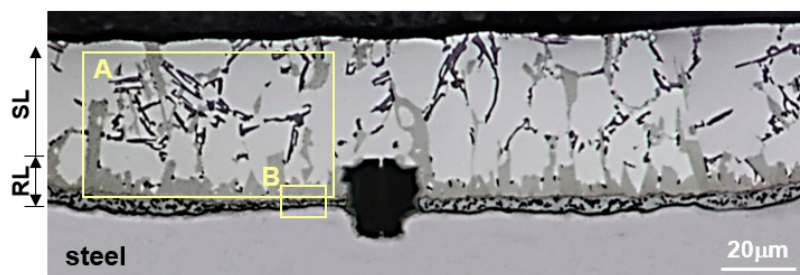


Figure 1. Optical microstructure of specimen hot-dipped at 690 °C for 2 min.

Figure 2 presents an SEM image of the area indicated by A in Figures 1 and 3 presents the results of the EBSD analysis. Given that EBSD was conducted in a non-etched state, the microstructure distribution was slightly different from that in the SEM image by re-polishing. Table 2 presents the results of the composition analysis of the phases labeled 1–11 in Figure 2 using EDS point analysis. The black needle-shaped phases 1–3 in Figure 2 represent Si. A small amount of Al was detected; however, Si did not dissolve in Al [25]. Hence, the detected Al represents the Al matrix in the EDS analysis results. In the EBSD results, the phase was Si, whereas the structures in the SEM image consisted of aggregates of fine grains, and the randomly shaped phases were parts of one grain. On the other hand, phases 4–11 exhibited a slight color difference when observed using an optical microscope and SEM. Moreover, phases 9–11 were reaction layer phases, as they were connected to the reaction layer. These phases were classified into two phase groups by EDS analysis. Phases 4–11 contained Al and Ni as the main components, but divided into two kinds: 4–6 in which Si and Fe are small in solid content and 7–11 phases in which Fe and Si contents are higher than those phases. From the EBSD results, phases 4–6 were Al_3Ni (orthorhombic). Furthermore, Al_3Ni was observed as a polygonal shape in the SEM image; however, from the EBSD results, it was found to be an aggregate of very fine grains. It was confirmed that phases 7–11 were Al_9FeNi (T, monoclinic) phases. In Figure 2, Figures 7 and 8, the Al_9FeNi (T) phases were present in the solidification layer, which were similar to the phase indicated by the red circle in Figure 3. Moreover, these were mostly observed near the reaction layer.

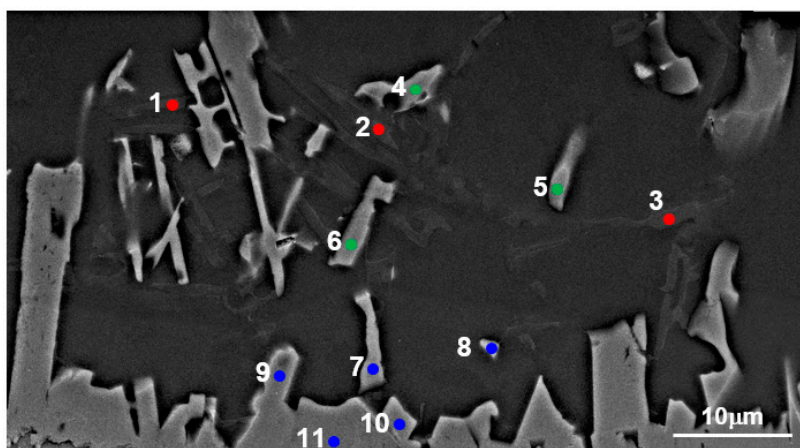


Figure 2. SEM image showing microstructure of area denoted as a rectangular “A” in Figure 1.

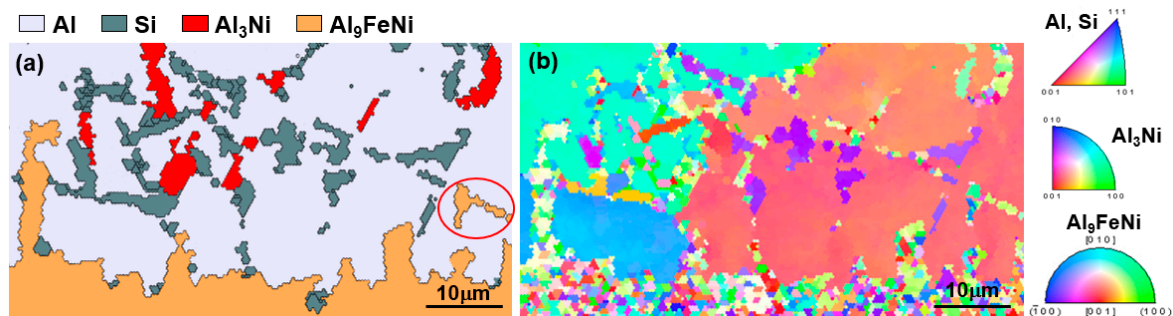


Figure 3. Electron backscatter diffraction (EBSD) analysis results using Chi-Scanning for the solidification layer (rectangular “A” in Figure 1): (a) Phase map and (b) inverse pole figure (IPF).

Table 2. Energy-dispersive X-ray spectroscopy (EDS) analysis results of phases denoted as 1–11 in Figure 2.

| No. | at%/wt% | Al | Ni | Si | Fe | Phase |
|-----|---------|------|------|------|------|-------------------------|
| 1 | at% | 11.5 | - | 88.5 | - | Si |
| | wt% | 11.1 | - | 88.9 | - | |
| 2 | at% | 5.3 | - | 94.7 | - | Si |
| | wt% | 5.1 | - | 94.9 | - | |
| 3 | at% | 6.0 | - | 94.0 | - | Si |
| | wt% | 5.8 | - | 94.2 | - | |
| 4 | at% | 82.5 | 15.9 | 1.1 | 0.5 | Al ₃ Ni |
| | wt% | 69.2 | 28.9 | 0.9 | 1.0 | |
| 5 | at% | 87.9 | 10.2 | 1.5 | 0.4 | Al ₃ Ni |
| | wt% | 78.1 | 19.8 | 1.4 | 0.7 | |
| 6 | at% | 84.4 | 12.8 | 2.1 | 0.7 | Al ₃ Ni |
| | wt% | 72.8 | 24.1 | 1.9 | 1.2 | |
| 7 | at% | 80.2 | 12.7 | 3.1 | 4.0 | Al ₉ FeNi(T) |
| | wt% | 67.2 | 23.1 | 2.7 | 7.0 | |
| 8 | at% | 81.5 | 13.0 | 1.0 | 4.5 | Al ₉ FeNi(T) |
| | wt% | 67.8 | 23.5 | 0.9 | 7.8 | |
| 9 | at% | 78.2 | 11.4 | 3.5 | 6.9 | Al ₉ FeNi(T) |
| | wt% | 64.7 | 0.5 | 3.0 | 11.8 | |
| 10 | at% | 80.1 | 10.3 | 2.1 | 7.5 | Al ₉ FeNi(T) |
| | wt% | 66.7 | 18.5 | 1.8 | 13.0 | |
| 11 | at% | 78.5 | 8.9 | 3.1 | 9.5 | Al ₉ FeNi(T) |
| | wt% | 65.0 | 16.0 | 2.7 | 16.3 | |

3.1.2. Microstructural Evolution of Solidification Layer

The formation of the Fe-containing phase in the solidification layer indicates that Fe was dissolved in the Al-7wt%Ni-6wt%Si liquid phase. Based on this, (Al-7wt%Ni-6wt%Si)-xFe pseudo-binary phase diagram was obtained using Thermo-CalcTM software, to evaluate the formation of a solidification layer under phase transformation during the cooling of the (Al-7wt%Ni-6wt%Si)-xFe liquid containing Fe.

Figure 4 presents the (Al-7wt%Ni-6wt%Si)-xFe pseudo-binary phase diagram obtained using Thermo-CalcTM software. In Figure 4, it can be seen that the phases formed during cooling vary depending on the Fe content. The Fe content during solidification was 0.92 wt% (0.46 at%), as measured using EDS. The phase changes occurring during cooling proceeded in the order of primary Al₃Ni + Liquid → Al₃Ni + Al + Liquid → Al₃Ni + τ₁ + Al + Liquid → Al₃Ni + τ₁ + Al + Si. On the other hand, given the dimensions of the supercooled specimen (thickness of 1.4 mm, width of 40 mm, and length of 120 mm), no phase transformation due to diffusion occurred at low temperatures.

In particular, when Al_3Ni and Al were preferentially formed at the initial stage of cooling, only Si was concentrated in the liquid; thus, Si was easily crystallized, and the τ_1 ($\text{Al}_2\text{Fe}_3\text{Si}_3$, triclinic) phase transformation degenerated. Hence, the solidification layer was considered to comprise Al_3Ni + Al + Si_3 phases. On the other hand, in Figure 4, when Fe was concentrated to approximately 1.3–2.0 wt%, the primary T phase could form during cooling, and even in the liquid. It was therefore considered that the solidification layer near the reaction layer contained a relatively high concentration of Fe; thus, an $\text{Al}_9\text{FeNi(T)}$ phase was generated.

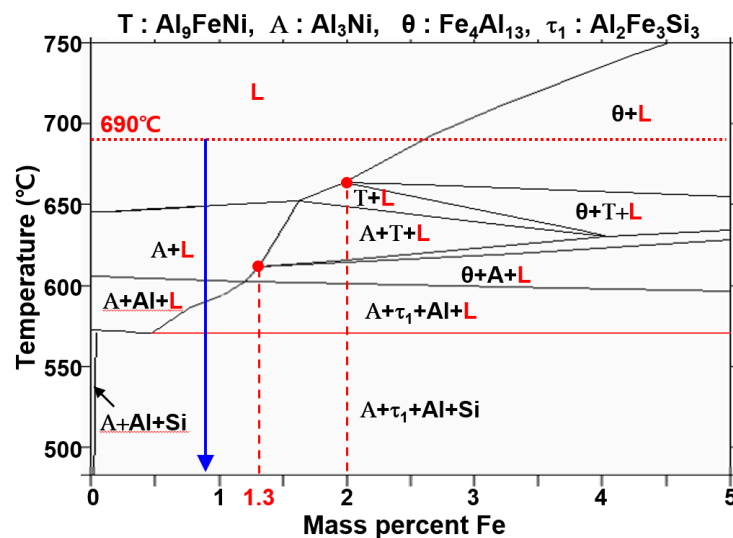


Figure 4. (Al-7Ni-6Si)-xFe (max. 5%) pseudo-binary phase diagram calculated using Thermo-CalcTM software.

3.2. Microstructure of Reaction Layer

3.2.1. Microstructural Identification of Reaction Layer

Figure 5 presents an SEM image, in which the reaction layer region indicated by B in Figure 1 is enlarged. The reaction layer can be classified into three layers (R1, R2, R3) and one phase (white phases in the R3 layer). Table 3 presents the results of the EDS point analysis of the phases labeled 1–5. There was a decrease in the quantitative reliability, given that the phases were very fine. However, the expected phase in Table 3 was qualitatively predicted from the composition.

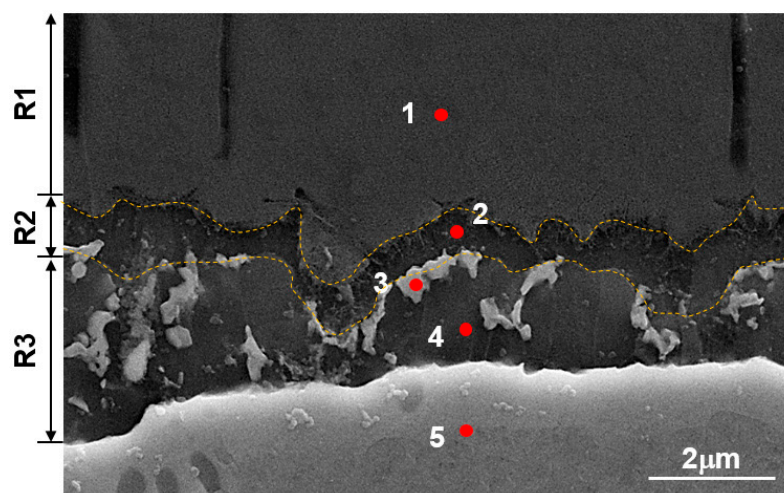


Figure 5. SEM image showing microstructure denoted as rectangular in Figure 1a and EDS analysis results of phases denoted as 1–5.

Table 3. EDS analysis results of phases denoted as 1–5 in Figure 5.

| No. | at%/wt% | Al | Ni | Si | Fe | Phase |
|-----|---------|------|------|------|------|--|
| 1 | at% | 79.0 | 14.3 | 0.6 | 6.1 | $\text{Al}_9\text{FeNi}(\text{T})$ |
| | wt% | 64.0 | 25.1 | 0.5 | 10.4 | |
| 2 | at% | 63.6 | 0.5 | 2.9 | 33.0 | $\text{Fe}_4\text{Al}_{13}(\theta)$ or $\text{Fe}_2\text{Al}_5(\eta)$ |
| | wt% | 46.8 | 0.7 | 2.2 | 50.3 | |
| 3 | at% | 38.9 | - | 18.5 | 42.6 | $\text{Al}_2\text{Fe}_3\text{Si}_3(\tau_1)$ |
| | wt% | 26.5 | - | 13.2 | 60.3 | |
| 4 | at% | 58.5 | 0.1 | 3.3 | 38.1 | $\text{Fe}_4\text{Al}_{13}(\theta)$ or $\text{Fe}_2\text{Al}_5(\eta)$ |
| | wt% | 41.5 | 0.1 | 2.5 | 55.9 | |
| 5 | at% | 0.1 | 1.3 | 1.0 | 97.6 | Fe |
| | wt% | 0.2 | 1.2 | 2.0 | 96.6 | |

To understand the composition, distribution, and grain size of the reaction layer, the TEM sample in Figure 1b (reactive layer region) was evaluated using FIB and observed by scanning transmission electron microscopy (STEM). Figure 6a,b present the high-angle annular dark-field (HAADF) and bright-field images, respectively, and Figure 6c is an enlarged HAADF image denoted as X in Figure 6a. Moreover, Figure 7 presents the EDS mapping analysis of Al, Ni, Si and Fe. From the Figure 7, the sample was divided into several regions, with respect to the concentrations of Al, Ni, Si and Fe. Table 4 presents the phase predictions from the EDS analysis of each area.

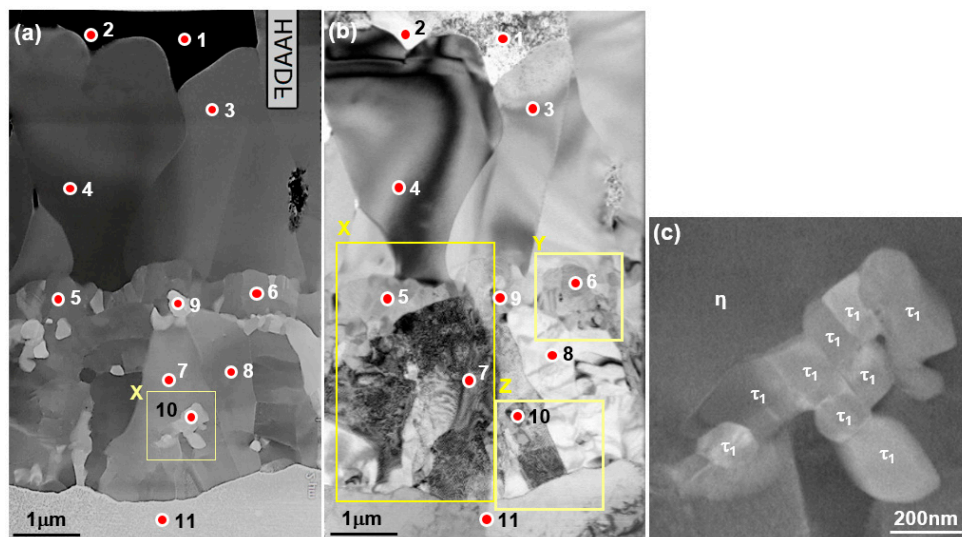
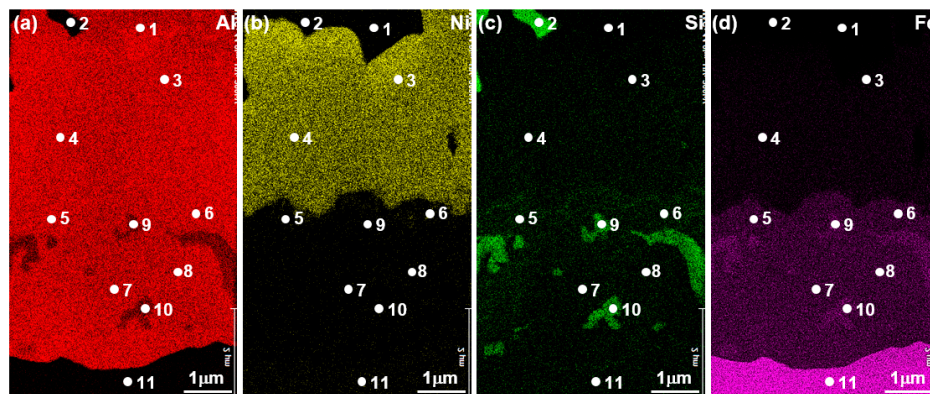
**Figure 6.** (a) HAADF image and (b) bright-field image of FE-TEM specimen for the area of reaction layer deflected by FIB; and (c) an enlarged image of the area indicated by X in Figure 6a.**Figure 7.** Results of EDS area-analysis of FE-TEM specimen: (a) Al, (b) Ni, (c) Si, and (d) Fe.

Table 4. EDS analysis results of phases denoted as 1–11 in Figures 6 and 7.

| No. | at%/wt% | Al | Ni | Si | Fe | Phase |
|-----|---------|------|------|------|------|--|
| 1 | at% | 98.5 | 0.3 | 1.0 | 0.2 | Al |
| | wt% | 98.0 | 0.6 | 1.0 | 0.4 | |
| 2 | at% | 5.3 | 1.1 | 93.5 | 0.1 | Si |
| | wt% | 5.1 | 2.3 | 92.5 | 0.1 | |
| 3 | at% | 79.7 | 11.6 | 1.7 | 7.0 | Al ₉ FeNi(T) |
| | wt% | 65.8 | 20.9 | 1.4 | 11.9 | |
| 4 | at% | 79.5 | 10.7 | 1.8 | 8.0 | Al ₉ FeNi(T) |
| | wt% | 65.5 | 19.3 | 1.5 | 13.7 | |
| 5 | at% | 73.1 | 0.1 | 3.6 | 23.2 | Fe ₄ Al ₁₃ (θ) |
| | wt% | 58.4 | 0.2 | 3.1 | 38.3 | |
| 6 | at% | 72.2 | - | 4.1 | 23.7 | Fe ₄ Al ₁₃ (θ) |
| | wt% | 57.5 | - | 3.4 | 39.1 | |
| 7 | at% | 71.6 | - | 2.6 | 25.8 | Fe ₂ Al ₅ (η) |
| | wt% | 56.1 | - | 2.1 | 41.8 | |
| 8 | at% | 71.8 | - | 1.7 | 26.5 | Fe ₂ Al ₅ (η) |
| | wt% | 56.0 | - | 1.4 | 42.6 | |
| 9 | at% | 32.6 | - | 31.7 | 35.7 | Al ₂ Fe ₃ Si ₃ (τ_1) |
| | wt% | 23.4 | - | 23.6 | 53.0 | |
| 10 | at% | 39.3 | - | 24.1 | 36.6 | Al ₂ Fe ₃ Si ₃ (τ_1) |
| | wt% | 28.0 | - | 17.9 | 54.1 | |
| 11 | at% | 0.7 | 0.6 | 0.8 | 97.9 | Fe |
| | wt% | 0.3 | 0.7 | 0.4 | 98.6 | |

Figure 8 presents the diffraction pattern of the EDS point analysis region labeled 1–11 in Figure 6. Phases 1 and 2 represent Al and Si, respectively, which were solidified layer structures. From the EDS point analysis, it was confirmed that phases 3 and 4, which grew along the solidification layer, were the Al₉FeNi (T, monoclinic) phase. It can be seen that the Al₉FeNi(T) phases had a relatively larger grain size than other phases, and the grain size on the side of the solidification layer was larger than that on the side of the base metal.

From the EDS point analysis, phases 5–8 consisted mainly of Al and Fe. Moreover, EDS mapping analysis revealed that the Fe concentration of phases 5 and 6, which were in close proximity to the T phases, was approximately 2 at% lower than that of phases 7 and 8, which were in close proximity to the steel side, and the Si concentration was approximately 2 at% higher. By diffraction pattern analysis, phases 5 and 6 were confirmed as a Fe₄Al₁₃ (θ , monoclinic) phase, and phases 7 and 8 were confirmed as a Fe₂Al₅ (η , orthorhombic) phase. Furthermore, labeled 9 and 10 in Figure 6a which appears as a white particle, is identified as Al₂Fe₃Si₃ (τ_1 , triclinic) phase. Figure 6c reveals that the τ_1 phases consist of several grains with diameters of 100–200 nm, rather than one grain.

Figure 9 presents a bright-field image, in which the X-Z region of Figure 6b is enlarged. Figure 9a,b are the enlarged images of the Al₉FeNi(T) phase layer. It can be seen that the Fe₄Al₁₃(θ) phase layer formed to a thickness of less than 1 μ m directly under the Al₉FeNi(T) phase layer. The grain diameter of the Fe₄Al₁₃(θ) phase adjacent to the Al₉FeNi(T) phase layer was 100–500 nm, and the grain diameter of the adjacent θ phase was approximately 200 nm. Most of the Fe₄Al₁₃(θ) phase was characterized by a twin formation. Moreover, between the Fe₄Al₁₃(θ) phase layer and the steel, an Fe₂Al₅(η) phase layer with a thickness of approximately 2.7 μ m was formed. The Fe₂Al₅(η) phase grain had a columnar shape (aspect ratio: 1.5) and twin formations in several grains (Figure 8c). Figure 9d presents an HR-TEM image of the D region in Figure 9c. A Fe₃AlC(κ , FCC) layer was formed on the Fe₂Al₅(η) phase layer/steel interface, with a thickness of approximately 10–15 nm.

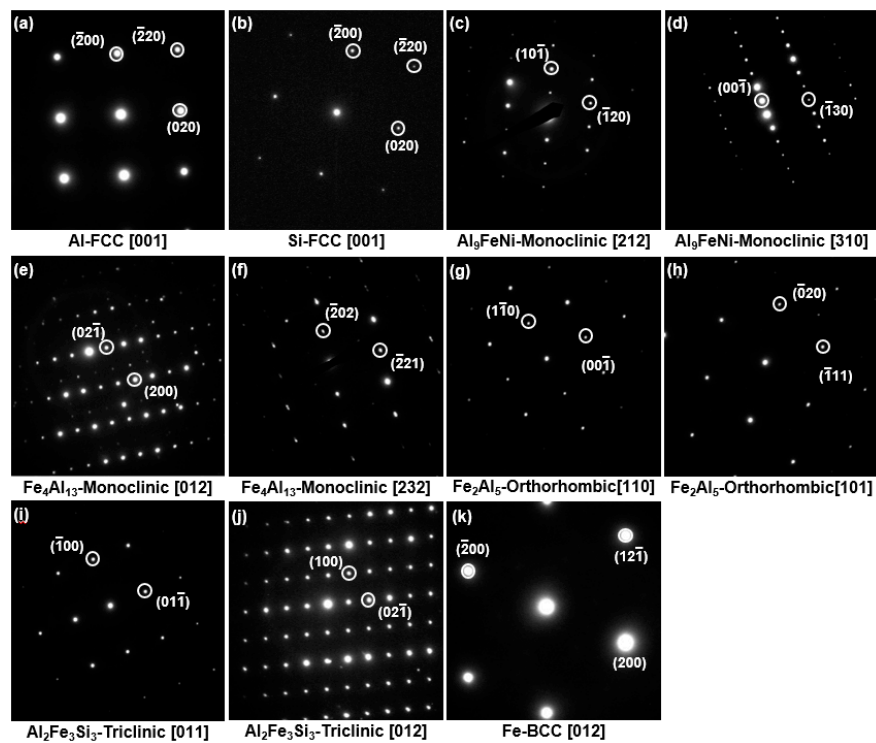


Figure 8. Diffraction patterns and those key diagram taking from area denoted as 1–11 in Figures 6 and 7, respectively. (a) Al, (b) Si, (c,d) Al₉FeNi(T), (e,f) Fe₄Al₁₃(θ), (g,h) Fe₂Al₅(η), (i,j) Al₂Fe₃Si₃(τ_1), (k) Fe.

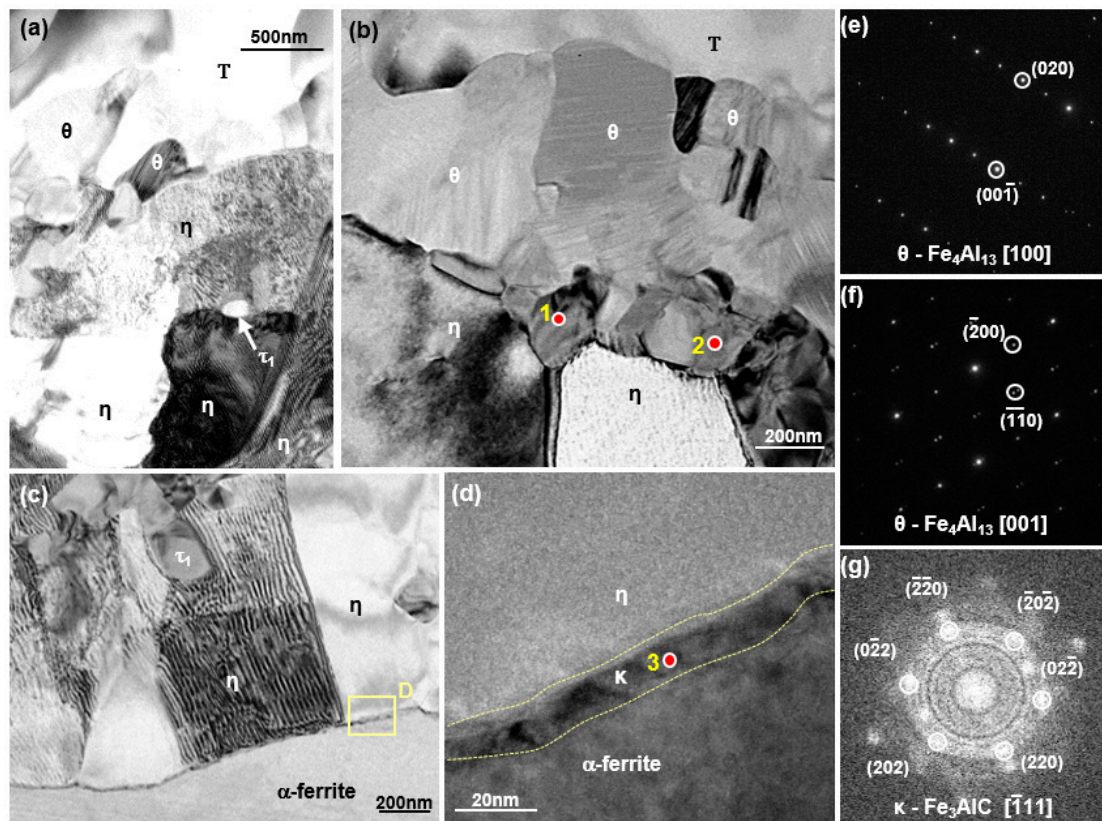


Figure 9. Bright-field images observed from rectangular area denoted as X-Z in Figure 6b: (a) X area, (b) Y area, (c) Z area, and (d) HR-TEM image observed from rectangular area denoted as D in (c) and (e–g) diffraction patterns and key diagram denoted as 1–3 in (b) and (d).

Figure 10 presents the EBSD analysis results for the reaction layer. Figure 10a is the phase map, and Figure 10b is the inverse pole figure (IPF). The reaction layer was formed in the order of the T/ θ / η layer on the solidification layer side. The very fine $\text{Al}_2\text{Fe}_3\text{Si}_3(\tau_1)$ phase and $\text{Fe}_3\text{AlC}(\kappa)$ phases observed by TEM were not detected by EBSD, and were simply classified as $\text{Fe}_2\text{Al}_5(\eta)$ phase layers. This suggests that EBSD analysis cannot accurately determine the size and distribution of the phase when the thickness of the reaction layer is 1 μm or less and the grain size is small.

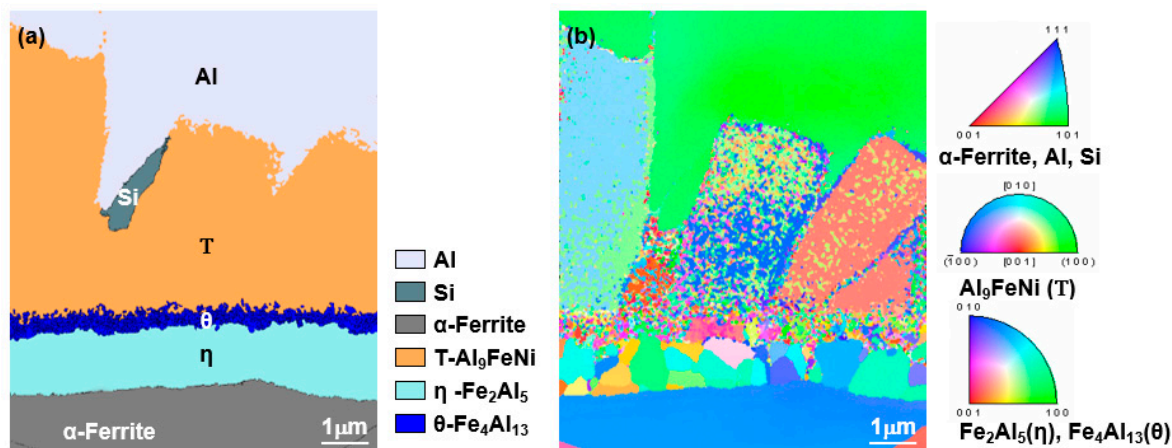


Figure 10. (a) Phase map and (b) IPF obtained from EBSD analysis using Chi-Scanning.

From the TEM observation and EBSD analysis results, it was confirmed that the reaction layer was formed in the order of $\text{Al}_9\text{FeNi}(\text{T}) \rightarrow \text{Fe}_4\text{Al}_{13}(\theta) \rightarrow \text{Fe}_2\text{Al}_5(\eta)$ from the solidification side, and the $\text{Al}_2\text{Fe}_3\text{Si}_3(\tau_1)$ phase was dispersed in the $\text{Fe}_2\text{Al}_5(\eta)$ phase layers. The characteristics of each phase are as follows. The $\text{Al}_9\text{FeNi}(\text{T})$ phase had a monoclinic crystal structure, and the grains on the solidification layer side were larger than those on the base material side. The $\text{Fe}_4\text{Al}_{13}(\theta)$ phase had a monoclinic crystal structure, and the grain diameter was approximately 100–500 nm. In addition, twin formations were observed. The $\text{Fe}_2\text{Al}_5(\eta)$ phase had an orthorhombic crystal structure, and the grains developed in a columnar shape. Moreover, many $\text{Fe}_2\text{Al}_5(\eta)$ grains contained twin formations. The $\text{Al}_2\text{Fe}_3\text{Si}_3(\tau_1)$ phase contained a triclinic crystal structure, and several grains with diameters of 100–200 nm were present. The $\text{Fe}_3\text{AlC}(\kappa)$ phase layer was formed with a thickness of approximately 10–15 nm at the $\text{Fe}_2\text{Al}_5(\eta)$ phase layer/steel interface.

3.2.2. Microstructural Evolution of Reaction Layer

Figure 11 presents a schematic diagram depicting the shape of the reaction phases and the reaction layer based on EBSD and TEM analyses of the plated layer. Al, Si, and Al_3Ni were the major phases in the solidification layer, and a small $\text{Al}_9\text{FeNi}(\text{T})$ phase was present near the reaction layer. The reaction layers were formed in the order of $\text{Al}_9\text{FeNi}(\text{T})$, $\text{Fe}_4\text{Al}_{13}(\theta)$, and $\text{Fe}_2\text{Al}_5(\eta)$ from the solidification side, and the average thicknesses of the respective phases were 4.7 μm , 500 nm and 2.0 μm . Moreover, $\text{Al}_2\text{Fe}_3\text{Si}_3(\tau_1)$ was present in $\text{Fe}_2\text{Al}_5(\eta)$. Si was also formed between the $\text{Al}_9\text{FeNi}(\text{T})$ phases, and the $\text{Fe}_3\text{AlC}(\kappa)$ layer was formed at the $\text{Fe}_2\text{Al}_5(\eta)$ layer/steel interface with a thickness of approximately 10–15 nm. Fine twin formations were present in the $\text{Fe}_4\text{Al}_{13}(\theta)$ grains, and twin formations were present in several $\text{Fe}_2\text{Al}_5(\eta)$ grains.

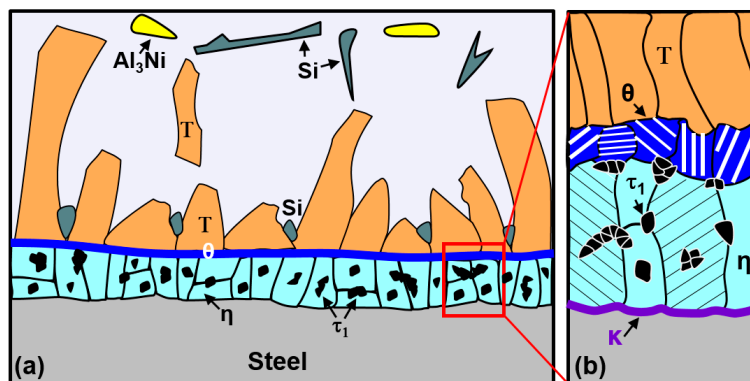


Figure 11. Schematic diagram of the distribution of phases in the solidification and reaction layers.

The microstructure of the Al-(5–10)wt%Si alloy hot-dipped coating layer without Ni was compared with that of the coating layer in the study, as no previous studies were conducted on the Al-Ni-Si alloy hot-dipped coating. For the Al-(5–10)wt% Si hot-dipped steel, the reaction layer was formed in the order of Al₇Fe₂Si(τ₅), Fe₄Al₁₃(θ), Fe₂Al₅(η) [23,26,27] or Al₇Fe₂Si(τ₅), and Fe₂Al₅(η) [28] in the solidification layer. Moreover, it was reported that Al₂Fe₃Si₃(τ₁) was formed within Fe₂Al₅(η) in common. Therefore, when Ni was added to the Al-Si coating, Al₉FeNi(T) was formed instead of Al₇Fe₂Si(τ₅), Fe₄Al₁₃(θ)/Fe₂Al₅(η) was formed in the lower layer, and Al₂Fe₃Si₃(τ₁) was formed in Fe₂Al₅(η).

From the phase diagram, the formation of the reaction layer in the order of Al₉FeNi(T), Fe₄Al₁₃(θ), Fe₂Al₅(η) in the solidification layer can be understood, in addition to the formation of Al₂Fe₃Si₃(τ₁) in Fe₂Al₅(η). Dipping the steel into a 690 °C Al-7wt%Ni-6wt%Si molten bath resulted in the partial dissolution of the steel. The reaction that occurred during hot-dipping at 690 °C was divided into two reactions: The reaction between the Al-7wt%Ni-6wt%Si melts and dissolved Fe, and the diffusion reaction between the reaction layer formed in the previous reaction and steel. The influence of the increase in the Fe concentration on the phase formed in the Al-7wt%Ni-6wt%Si molten metal was therefore analyzed using a (Al-7wt%Ni-6wt%Si)-xFe pseudo-binary phase diagram.

Figure 12 presents the (Al-7wt%Ni-6wt%Si)-xFe pseudo-binary phase diagram obtained using Thermo-Calc™ software. Figure 12 reveals that solid Fe₄Al₁₃(θ) can be formed when Fe concentration of over 2.63 wt% is hot-dipped into the Al-7wt%Ni-6wt%Si molten metal at 690 °C. When the Fe concentration was greater than 10.0 wt%, Fe₄Al₁₃(θ) and Al₉FeNi(T) can be formed, and when the Fe concentration was greater than 29.0 wt%, three phases of Fe₄Al₁₃(θ), Al₃Ni, and Al₂Fe₃Si₃(τ₁) can be formed. In this study, Al₃Ni was not formed in the reaction layer, and was only present in the solidification layer. Given that Al₃Ni was not observed in the reaction layer, it was expected that the Fe concentration in the molten metal near the steel during coating was 29 wt% or lower. In addition, when the Fe concentration in the molten metal increased, θ first crystallized, and then T crystallized as the reaction progressed. This may be why the T layer was formed near the liquid phase, and the Fe₄Al₁₃(θ) layer was formed below the Al₉FeNi(T) layer.

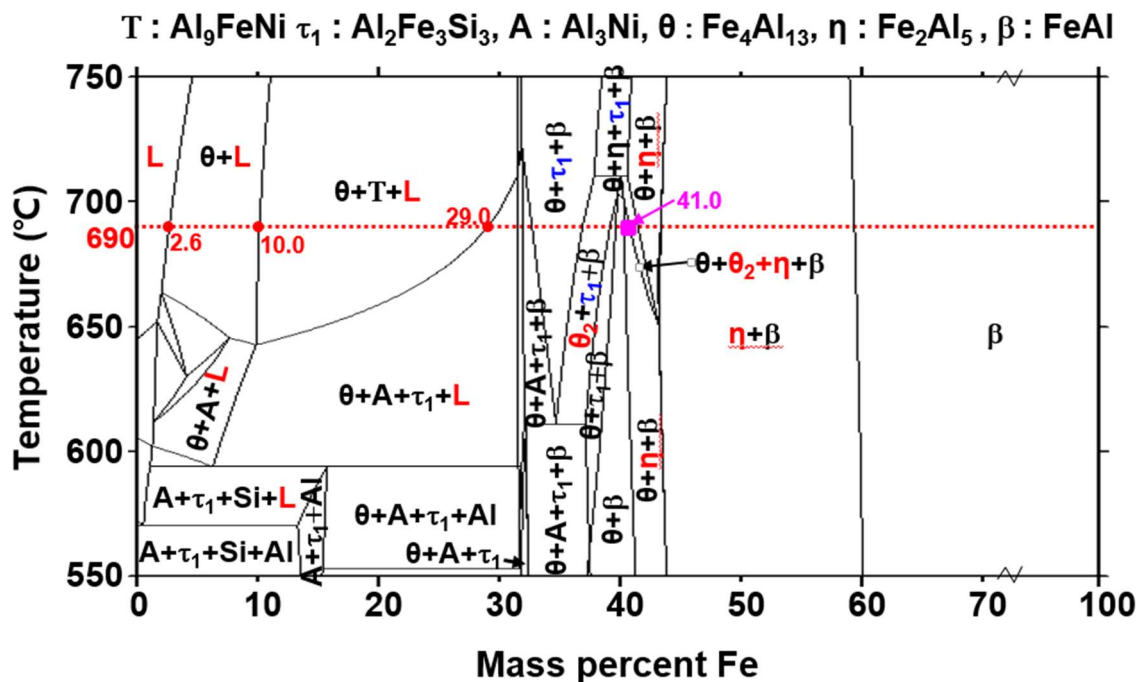


Figure 12. (Al-7wt%Ni-6wt%Si)-xFe pseudo-binary phase diagram obtained using Thermo-CalcTM software.

Table 5 presents the equilibrium phase composition at 690 °C in the (Al-7wt%Ni-6wt%Si)-xFe system obtained using Thermo-CalcTM software. With reference to Table 5, Si was not dissolved in $\text{Al}_9\text{FeNi(T)}$. During the formation and development of $\text{Al}_9\text{FeNi(T)}$ in the molten metal, Si phases were formed around $\text{Al}_9\text{FeNi(T)}$, due to the discharge and agglomeration of Si from $\text{Al}_9\text{FeNi(T)}$.

Table 5. Equilibrium concentration of phases at 690 °C calculated using Thermo-CalcTM software.

| Phase at 690 °C | at%/wt% | Al | Ni | Si | Fe |
|--|---------|------|------|------|------|
| T - Al_9FeNi | at% | 81.9 | 7.6 | - | 10.5 |
| | wt% | 68.0 | 13.8 | - | 18.2 |
| θ_1 - $\text{Fe}_4\text{Al}_{13}$ | at% | 76.1 | 3.9 | - | 20.0 |
| | wt% | 60.4 | 6.7 | - | 32.9 |
| θ_2 - $\text{Fe}_4\text{Al}_{13}$ | at% | 73.3 | - | 3.3 | 23.4 |
| | wt% | 58.6 | - | 2.7 | 38.7 |
| η - Fe_2Al_5 | at% | 68.9 | 1.4 | 2.8 | 26.9 |
| | wt% | 52.7 | 2.4 | 2.2 | 42.7 |
| β - FeAl | at% | 41.8 | 2.8 | 11.7 | 43.7 |
| | wt% | 27.8 | 4.0 | 8.1 | 60.1 |
| τ_1 - $\text{Al}_2\text{Fe}_3\text{Si}_3$ | at% | 63.1 | - | 14.7 | 22.2 |
| | wt% | 50.8 | - | 12.2 | 37.0 |

The formation mechanism of $\text{Fe}_2\text{Al}_5(\eta)$ was examined using the (Al-7wt%Ni-6wt%Si)-xFe pseudo-binary phase diagram. Given that the Fe concentration at which the $\text{Fe}_2\text{Al}_5(\eta)$ was formed at 690 °C was approximately 41.0 wt% (as indicated by the pink rectangular in Figure 12), $\text{Fe}_2\text{Al}_5(\eta)$ could not be formed by dissolving Fe in the liquid phase during coating at 690 °C. Another mechanism by which $\text{Fe}_2\text{Al}_5(\eta)$ could be formed as the solid phase diffusion reaction between the already formed reaction phase ($\text{Fe}_4\text{Al}_{13}(\theta)$, $\text{Al}_9\text{FeNi(T)}$) and steel. In particular, $\text{Fe}_2\text{Al}_5(\eta)$ can be formed through mutual diffusion when Al, Ni, and Si are diffused into the steel in the molten metal $\rightarrow \text{Al}_9\text{FeNi(T)} \rightarrow \text{Fe}_4\text{Al}_{13}(\theta)$ path, and Fe is diffused through the reaction layer steel $\text{Fe}_4\text{Al}_{13}(\theta) \rightarrow \text{Al}_9\text{FeNi(T)} \rightarrow$ molten metal path. There are three phases that can be formed on the steel side by mutual diffusion in the state diagram, namely, FeAl(β), $\text{Fe}_2\text{Al}_5(\eta)$, and $\text{Al}_2\text{Fe}_3\text{Si}_3(\tau_1)$.

In this diffusion mechanism, the phase with the smallest concentration difference in comparison with $\text{Fe}_4\text{Al}_{13}(\theta)$ is easily formed. Therefore, $\text{Fe}_2\text{Al}_5(\eta)$ in Table 5 is most similar to $\text{Fe}_4\text{Al}_{13}(\theta)$ and Al and Fe concentrations. In Figure 9b, it can be seen that the grain size of $\text{Fe}_4\text{Al}_{13}(\theta)$ adjacent to $\text{Fe}_2\text{Al}_5(\eta)$ was significantly smaller than that of $\text{Fe}_4\text{Al}_{13}(\theta)$ adjacent to the $\text{Al}_9\text{FeNi}(\text{T})$ layer. This is expected that the $\text{Fe}_4\text{Al}_{13}(\theta)$ grain decreased in size and disappeared, as it was transformed into $\text{Fe}_2\text{Al}_5(\eta)$ by the diffusion reaction.

The mechanism by which $\text{Al}_2\text{Fe}_3\text{Si}_3(\tau_1)$ was produced within $\text{Fe}_2\text{Al}_5(\eta)$ is as follows. $\text{Al}_9\text{FeNi}(\text{T})$ and $\text{Fe}_4\text{Al}_{13}(\theta)$ formed at Fe concentrations below 30 wt% did not dissolve Si, as can be seen in Table 5. Therefore, when $\text{Al}_9\text{FeNi}(\text{T})$ and $\text{Fe}_4\text{Al}_{13}(\theta)$ discharged Si into the liquid phase, the Si phase was formed in the solidification layer. However, when Si was discharged toward the steel, $\text{Al}_2\text{Fe}_3\text{Si}_3(\tau_1)$ phases that contained Si were precipitated. In Figures 6 and 7, the significant formation of $\text{Al}_2\text{Fe}_3\text{Si}_3(\tau_1)$ phases at the $\text{Fe}_4\text{Al}_{13}(\theta)/\text{Fe}_2\text{Al}_5(\eta)$ interface can be explained by the formation mechanism of the $\text{Al}_2\text{Fe}_3\text{Si}_3(\tau_1)$ phases.

Another reaction phase is the $\text{Fe}_3\text{AlC}(\kappa)$ formed at the $\text{Fe}_2\text{Al}_5(\eta)/\text{steel}$ interface. Springer recently reported that an 800 nm band that consists of $\text{FeAl}(\beta')$ and $\text{Fe}_3\text{AlC}(\kappa)$ phases was formed between the steel and $\text{Fe}_2\text{Al}_5(\eta)$ phase by inter-diffusion in the solid reaction of low-carbon steel and pure Al at 600 °C; however, there was no mention of the formation mechanism [27]. In Figure 13, carbon was not detected in the $\text{Al}_9\text{FeNi}(\text{T})$ and $\text{Fe}_2\text{Al}_5(\eta)$ layers. This confirms that the carbon solubility of $\text{Al}_9\text{FeNi}(\text{T})$ and $\text{Fe}_2\text{Al}_5(\eta)$ was very low. Given that the boron steel used in the study contained 0.22 wt% of carbon, it was suggested that the $\text{Fe}_3\text{AlC}(\kappa)$ layer was formed by carbon accumulation that discharged in the $\text{Fe}_2\text{Al}_5(\eta)$ region transformed from steel to $\text{Fe}_2\text{Al}_5(\eta)$. A study of pure Al [29] and the Al-7Ni [15] hot-dip coating on boron steels similarly reported the formation of a $\text{Fe}_3\text{AlC}(\kappa)$ layer at the grain boundaries of $\text{Fe}_2\text{Al}_5(\eta)$ and adjacent steels.

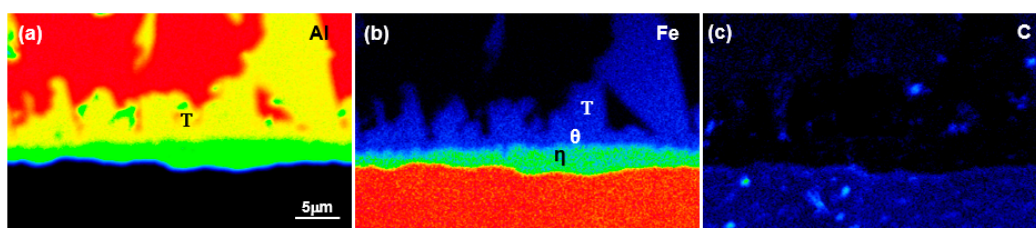


Figure 13. Electron probe micro-analysis (EPMA) area analysis near the reaction layer: (a) Al, (b) Fe, and (c) C.

During the formation of the reaction layer, It is expected that streaks occurred in the $\text{Fe}_4\text{Al}_{13}(\theta)$ and $\text{Fe}_2\text{Al}_5(\eta)$ phases, as can be seen in Figure 9b. Streaks in each θ and some η grain are observed at regular intervals throughout the grain, not in only one specific part. And it also has a different orientation, like each grain's crystal orientation. Hence, streaks are expected to twin. Takata et al. reported that during the interfacial reaction between liquid-Al and solid-Fe, strain developed due to the volume expansion in the process of transformation from α -ferrite to the η phase, which resulted in the refinement of the η phase in contact with the liquid phase [30]. In this study, it was considered that the twin formation in $\text{Fe}_4\text{Al}_{13}(\theta)$ and $\text{Fe}_2\text{Al}_5(\eta)$ between the $\text{Al}_9\text{FeNi}(\text{T})$ and steel was caused by the strain generated by the lattice transformation ($\text{Al}_9\text{FeNi}(\text{T}) \rightarrow \text{Fe}_4\text{Al}_{13}(\theta)$, $\text{Fe}_4\text{Al}_{13}(\theta) \rightarrow \text{Fe}_2\text{Al}_5(\eta)$) that occurred in the layer interface. Moreover, T and θ have the same monoclinic structure, but their space group is different ($\text{Al}_9\text{FeNi}(\text{T})$: P21/C [31], $\text{Fe}_4\text{Al}_{13}(\theta)$: C1/m1(12) [32]). The twin formation can be attributed to the expansion caused by the $\text{Al}_9\text{FeNi}(\text{T}) \rightarrow \text{Fe}_4\text{Al}_{13}(\theta)$ transformation.

4. Conclusions

The microstructures of the reaction layer and phases formed on boron steel hot-dipped in Al-7wt%Ni-6wt%Si were investigated using FIB, TEM, and EBSD. The formation mechanism of

each phase was examined by employing a (Al-7wt%Ni-6wt%Si)-xFe pseudo-binary phase diagram obtained using Thermo-CalcTM software. The results are as follows.

- (1) The solidification layer consisted mainly of Al, Al₃Ni, and Si phases, and a small Al₉FeNi(T) phase was observed near the reaction layer. By analyzing the solidification process using a phase diagram, it was found that three phases (Al, Al₃Ni and Si) were formed in the low Fe concentration region (0.92 wt% of Fe). Moreover, a T phase was formed during cooling in the high Fe concentration region (1.3 wt% of Fe or higher).
- (2) The reaction layers were formed in the order of Al₉FeNi(T), Fe₄Al₁₃(θ), and Fe₂Al₅(η) from the solidification side, and the average thicknesses of the phases were 4.7 μm, 500 nm and 2.0 μm, respectively. Moreover, Si was formed around the T phase, and the Fe₃AlC(κ) layer was formed at the Fe₂Al₅(η) layer/steel interface with a thickness of approximately 10–15 nm.
- (3) The Al₉FeNi(T) phase possessed a monoclinic crystal structure (space group: P21/C), and the grains on the side of the solidification layer were larger than those on the side of the base metal. The Fe₄Al₁₃(θ) phase possessed a monoclinic crystal structure (space group: C1/m1(12)), the grain diameter was approximately 100–500 nm, and twin formations were present. By analyzing the formation mechanisms using the (Al-7wt%Ni-6wt%Si)-xFe pseudo-binary phase diagram, it was confirmed that Fe₄Al₁₃(θ) was formed by the dissolution reaction of Fe in the liquid phase. Moreover, Fe₄Al₁₃(θ) can be formed when the Fe concentration exceeds 2.63 wt% in the 690 °C Al-7wt%Ni-6wt%Si molten metal. When the concentration of Fe increased to 10.0–29.0 wt%, isothermal solidification occurred in the Fe₄Al₁₃(θ) and Al₉FeNi(T) phases simultaneously. Moreover, given that the T phase did not dissolve Si, it was discharged, and the Si phase was formed around the T phase.
- (4) Fe₂Al₅(η) was interpreted from the phase diagram as being formed by a diffusion reaction between Fe₄Al₁₃(θ) and steel, not a dissolution reaction. Given that the difference in the compositions of Fe₄Al₁₃(θ) and Fe₂Al₅(η) was the smallest, Fe₄Al₁₃(θ) was transformed into Fe₂Al₅(η) by mutual diffusion. This was confirmed by the grain size of Fe₄Al₁₃(θ) adjacent to Fe₂Al₅(η), which was significantly smaller than that of Fe₄Al₁₃(θ) adjacent to Al₉FeNi(T). Moreover, given that Fe₄Al₁₃(θ) does not exhibit Si solubility, Si was discharged into Fe₂Al₅(η) or steel. Hence, Al₂Fe₃Si₃(τ₁), which contained a large amount of Si, was precipitated. This is consistent with the formation of Al₂Fe₃Si₃(τ₁), especially at the Fe₄Al₁₃(θ)/Fe₂Al₅(η) interface.
- (5) The Fe₃AlC(κ) layer was formed by carbon accumulation that discharged in the Fe₂Al₅(η) region transformed from steel to Fe₂Al₅(η).
- (6) The twin formations in the Fe₄Al₁₃(θ) and Fe₂Al₅(η) grains were due to strains caused by the lattice transformation (Al₉FeNi(T)→Fe₄Al₁₃(θ), Fe₄Al₁₃(θ)→Fe₂Al₅(η)) in the constrained state, wherein these phases were present between the Al₉FeNi(T) layer and steel.

Author Contributions: J.-Y.L., H.H., N.K. and C.-Y.K. conceived and designed the experiments; J.-Y.L. and H.H. performed the experiments; N.K. and J.-Y.L. analyzed the data; and J.-Y.L. and C.-Y.K. wrote the paper.

Funding: This work was supported by the National Research Foundation of Korea (NRF) grant funded by the Korean government (MSIP) through the Engineering Research Center (No. 2012R1A5A1048294).

Conflicts of Interest: The authors declare no conflict of interest. The funding sponsors had no role in the design of the study; the collection, analyses, or interpretation of data; the writing of the manuscript, or in the decision to publish the results.

References

1. Aranda, L.G.; Ravier, P.; Chastel, Y. Hot Stamping of Quenchable Steels: Material Data and Process Simulations. In Proceedings of the IDDRG, Bled, Slovenia, 11–14 May 2003; pp. 164–166.
2. Vaissiere, L.; Laurent, J.; Reinhardt, A. Development of Pre-Coated Boron Steel for Applications on psa Peugeot Citroen and Renault Bodies in White. *SAE Tech. Pap.* **2002**. [[CrossRef](#)]

3. Mega, T.; Hasegawa, K.; Kawabe, H. Ultra high-strength steel sheets for bodies, reinforcement parts, and seat frame parts of automobile—Ultra high-strength steel sheets leading to great improvement in crash-worthiness. *JFE Tech. Rep.* **2004**, *4*, 38–43.
4. Kolleck, R.; Veit, R.; Merklein, M.; Lechler, J.; Geiger, M. Investigation on induction heating for hot stamping of boron alloyed steels. *CIRP Ann.* **2009**, *58*, 275–278. [[CrossRef](#)]
5. Liu, H.; Xing, Z.; Bao, J.; Song, B. Investigation of the hot-stamping process for advanced high-strength steel sheet by numerical simulation. *J. Mater. Eng. Perform.* **2010**, *19*, 325–334. [[CrossRef](#)]
6. Kobayashi, S.; Yakou, T. Control of intermetallic compound layers at interface between steel and aluminum by diffusion-treatment. *Mater. Sci. Eng. A* **2002**, *338*, 44–53. [[CrossRef](#)]
7. Chang, Y.-Y.; Tsaur, C.-C.; Rock, J.C. Microstructure studies of an aluminide coating on 9Cr-1Mo steel during high temperature oxidation. *Surf. Coat. Technol.* **2006**, *200*, 6588–6593. [[CrossRef](#)]
8. Wang, C.-J.; Chen, S.-M. The high-temperature oxidation behavior of hot-dipping Al-Si coating on low carbon steel. *Surf. Coat. Technol.* **2006**, *200*, 6601–6605. [[CrossRef](#)]
9. Jarnverk Ab, N. Manufacturing of a hardened steel article. UK Patent GB1490535, 2 November 1977.
10. Ehling, W.; Cretteur, L.; Pic, A.; Vierstraete, R.; Yin, Q. Development of a Laser Decoating Process for Fully Functional al-si Coated Press Hardened Steel Laser Welded Blank Solutions. In Proceedings of the 5th International WLT-Conference on Lasers in Manufacturing 2009, Munich, Germany, 15–18 June 2009; p. 6.
11. Jung, B.-H.; Kong, J.-P.; Kang, C.-Y. Effect of hot-stamping heat treatment on microstructure and hardness in TWB laser joints of Al-Si-coated boron steel and Zn-coated DP steel. *Korean J. Metals Mater.* **2012**, *50*, 224–232.
12. Oh, M.-H.; Kong, J.-P.; Kwon, M.-S.; Kang, C.-Y. Effect of hot-stamping on microstructures and tensile properties of Al-Si coated boron steel welds with laser source. *J. Weld. Join.* **2013**, *31*, 96–106. [[CrossRef](#)]
13. Yoon, T.-J.; Oh, M.-H.; Shin, H.-J.; Kang, C.-Y. Comparison of microstructure and phase transformation of laser-welded joints in Al-10wt% Si-coated boron steel before and after hot stamping. *Mater. Charact.* **2017**, *128*, 195–202. [[CrossRef](#)]
14. Kwak, S.-Y.; Yun, J.-G.; Lee, J.-H.; Shin, D.-I.; Kang, C.-Y. Identification of intermetallic compounds and its formation mechanism in boron steel hot-dipped in Al-7 wt.% Mn alloy. *Coatings* **2017**, *7*, 222. [[CrossRef](#)]
15. Lee, J.-H.; Yun, J.-G.; Kwak, S.-Y.; Kang, C.-Y. Nucleation and growth of intermetallic compounds formed in boron steel hot-dipped in Al-Ni alloy. *Coatings* **2017**, *7*, 195. [[CrossRef](#)]
16. Eggeler, G.; Auer, W.; Kaesche, H. On the influence of silicon on the growth of the alloy layer during hot dip aluminizing. *J. Mater. Sci.* **1986**, *21*, 3348–3350. [[CrossRef](#)]
17. Akdeniz, M.V.; Mekhrabov, A.O.; Yilmaz, T. The role of si addition on the interfacial interaction in Fe-Al diffusion layer. *Scr. Metall. Mater.* **1994**, *31*, 1723–1728. [[CrossRef](#)]
18. Shady, M.; El-Sissi, A.; Attia, A.; El-Mahallawy, N.; Taha, M.; Reif, W. On the technological properties of steel strips aluminized in Al-Si baths. *J. Mater. Sci. Lett.* **1996**, *15*, 1032–1036. [[CrossRef](#)]
19. Heumann, T.; Dittrich, S. Über die kinetik der reaktion von festem und flüssigem aluminium mit eisen. *Z. Metall.* **1959**, *50*, 617–625.
20. Lemmens, B.; Springer, H.; Duarte, M.J.; De Graeve, I.; De Strycker, J.; Raabe, D.; Verbeken, K. Atom probe tomography of intermetallic phases and interfaces formed in dissimilar joining between Al alloys and steel. *Mater. Charact.* **2016**, *120*, 268–272. [[CrossRef](#)]
21. Shankar, S.; Apelian, D. Die soldering: Mechanism of the interface reaction between molten aluminum alloy and tool steel. *Metall. Mater. Trans. B* **2002**, *33*, 465–476. [[CrossRef](#)]
22. Zhang, K.; Bian, X.; Li, Y.; Liu, Y.; Yang, C. New evidence for the formation and growth mechanism of the intermetallic phase formed at the Al/Fe interface. *J. Mater. Res.* **2013**, *28*, 3279–3287. [[CrossRef](#)]
23. Lemmens, B.; Springer, H.; De Graeve, I.; De Strycker, J.; Raabe, D.; Verbeken, K. Effect of silicon on the microstructure and growth kinetics of intermetallic phases formed during hot-dip aluminizing of ferritic steel. *Surf. Coat. Technol.* **2017**, 104–109. [[CrossRef](#)]
24. Yun, J.-G.; Lee, J.-H.; Kwak, S.-Y.; Kang, C.-Y. Study on the formation of reaction phase to Si addition in boron steel hot-dipped in Al-7Ni alloy. *Coatings* **2017**, *7*, 186. [[CrossRef](#)]
25. Handbook, A. Alloy phase diagrams. *ASM Int.* **1992**, *3*, 2–319.
26. Cheng, W.-J.; Wang, C.-J. Microstructural evolution of intermetallic layer in hot-dipped aluminide mild steel with silicon addition. *Surf. Coat. Technol.* **2011**, *205*, 4726–4731. [[CrossRef](#)]

27. Springer, H.; Kostka, A.; Payton, E.; Raabe, D.; Kaysser-Pyzalla, A.; Eggeler, G. On the formation and growth of intermetallic phases during interdiffusion between low-carbon steel and aluminum alloys. *Acta Mater.* **2011**, *59*, 1586–1600. [[CrossRef](#)]
28. Gui, Z.-X.; Liang, W.-K.; Liu, Y.; Zhang, Y.-S. Thermo-mechanical behavior of the Al–Si alloy coated hot stamping boron steel. *Mater. Des.* **2014**, *60*, 26–33. [[CrossRef](#)]
29. Shin, D.; Lee, J.-Y.; Heo, H.; Kang, C.-Y. Formation procedure of reaction phases in Al hot dipping process of steel. *Metals* **2018**, *8*, 820. [[CrossRef](#)]
30. Takata, N.; Nishimoto, M.; Kobayashi, S.; Takeyama, M. Crystallography of Fe₂Al₅ phase at the interface between solid Fe and liquid Al. *Intermetallics* **2015**, *67*, 1–11. [[CrossRef](#)]
31. Pearson, W.B. *A handbook of Lattice Spacings and Structures of Metals and Alloys*—2; Pergamon: London, UK, 1967.
32. Black, P. The structure of FeAl₃. II. *Acta Crystallogr.* **1955**, *8*, 175–182. [[CrossRef](#)]



© 2018 by the authors. Licensee MDPI, Basel, Switzerland. This article is an open access article distributed under the terms and conditions of the Creative Commons Attribution (CC BY) license (<http://creativecommons.org/licenses/by/4.0/>).